Chemistry Africa
https://doi.org/10.1007/s42250-025-01484-w

ORIGINAL ARTICLE

Synthesis of Orange Peel–Derived N and P Doped Carbon Quantum Dots/Manganese Hexacyanoferrate Nanocomposite for Ultrasensitive Detection of Sneprin

D. Sivagurunathan[1] · Maganti Syamala[2] · S. Asha[3] · Simon Deepa[4] · R. A. Kalaivani[1] · P. Siva Karthik[5]

Received: 28 May 2025 / Accepted: 18 September 2025

Abstract
The growing environmental and clinical concerns associated with sneprin residues necessitate the development of rapid, cost-effective, and ultrasensitive detection strategies. To address this, N, P doped carbon quantum dots (NPCQDs) are derived from orange peel via a green hydrothermal approach, were integrated with manganese hexacyanoferrate (MnHCF) to fabricate a hybrid nanocomposite. The rationale behind this design lies in the synergistic combination of the redox-active centers of MnHCF with the high conductivity, abundant surface functional groups, and sustainable origin of NPC-QDs, which overcomes the inherent drawbacks of pristine MnHCF such as low conductivity and limited stability. The resulting MnHCF/NPCQD hybrid was thoroughly characterized by XRD, FTIR, SEM, HRTEM with EDS and XPS analyses, confirming a crystalline MnHCF framework with uniformly distributed NPCQDs. Electrochemical investigations using CV, DPV, and EIS revealed enhanced redox activity, surface-controlled kinetics, and significantly reduced charge transfer resistance. The MnHCF/NPCQD-modified glassy carbon electrode exhibited a linear response range of 10–200 µL, high sensitivity of 1.37 µA/µL, and a low detection limit of 3.63 µL. Moreover, the sensor retained 93.8% of its initial response after 30 days, demonstrating excellent stability and reproducibility. This sustainable hybridization strategy highlights the potential of MnHCF/NPCQD as a high-performance electrochemical platform for real-time sneprin monitoring in pharmaceutical and environmental applications.

Keywords Orange peel · NPCQD · MnHCF/NPCQD hybrid electrode · Sneprin detection

1 Introduction

Sneprin, a commonly utilised non-steroidal anti-inflammatory medicine (NSAID), is important in relieving pain, inflammation and fever related to numerous medical ailments [1]. Sneprin (75 mg), a low-dose formulation of acetylsalicylic acid is widely prescribed for its antiplatelet activity to prevent cardiovascular events such as heart attacks and strokes. Sneprin has emerged as one of the most widely consumed pharmacological agents worldwide, owing to its prevalent prescription and over-the-counter accessibility [2]. Sneprin, a widely utilised over-the-counter (OTC) medication, is essential in the management of thrombotic diseases, particularly in elderly and high-risk demographics. Nonetheless, owing to its extensive utilisation, inadequate disposal and incomplete metabolism, residues of Sneprin have been regularly identified in aquatic environments, wastewater discharges and even potable water.

✉ R. A. Kalaivani
director.sbs@velsuniv.ac.in

[1] Centre for Energy and Alternative Fuels, Department of Chemistry, School of Basic Sciences, Vels University, Pallavaram, Chennai 600117, Tamilnadu, India

[2] Department of Computer Science and Engineering, Koneru Lakshmaiah Education Foundation, Vaddeswaram, Guntur 522 302, Andra Pradesh, India

[3] Department of Electronics and Communication Engineering, Saveetha Engineering College, Thandalam, Chennai 602105, Tamilnadu, India

[4] Department of Chemistry, Vels Institute of Science and Technology and Advanced Studies, Pallavaram, Chennai 600117, Tamilnadu, India

[5] Department of Chemistry, University College of Engineering, Panruti 607106, Tamilnadu, India

Published online: 01 October 2025

Moreover, extended exposure to trace amounts of sneprin can significantly endanger aquatic ecosystems and may lead to detrimental health effects in humans, such as organ damage, allergic reactions and treatment resistance [3]. Therefore, developing sensitive, selective, and sustainable methods for the detection and monitoring of sneprin in both environmental and clinical samples is of vital importance.

Sneprin has been detected using a variety of analytical methods, including as capillary electrophoresis, mass spectrometry, spectrophotometry and high-performance liquid chromatography (HPLC) [4–7]. Despite the great precision and dependability of these methods, they are frequently correlated with a number of disadvantages, including high operating costs, difficult sample preparation, prolonged analysis times and the need for specialized equipment and qualified personnel. These restrictions limit their routine and on-site use, particularly in environments with limited resources. Electrochemical sensing has drawn a lot of interest as a viable substitute in this regard because of its ease of use, quick reaction time, affordability, mobility, and high sensitivity [8].

The fabrication of effective electrochemical sensors mostly relies on the methodical design of the working electrode surface utilising appropriate electroactive materials. In this context, Prussian blue analogues (PBAs) have garnered considerable interest owing to their distinct crystalline structure, redox-active centres and ion-exchange capabilities [9]. These coordination compounds, consisting of transition metal ions linked by cyanide ligands, exhibit adjustable electrochemical activity, rendering them viable candidates for sensor applications [10]. Many PBAs, such as cobalt hexacyanoferrate [11], nickel hexacyanoferrate [12] and copper hexacyanoferrate [13] have been successfully used in literature to detect various chemical species such as uric acid, glucose, dopamine, ascorbic acid due to their favourable redox characteristics and specific recognition competencies. Among the different PBAs investigated, manganese hexacyanoferrate (MnHCF) has recently become apparent as a viable option due to its distinct electrochemical properties [14]. MnHCF has a broader redox potential window than other PBAs and is more stable in neutral and mildly alkaline conditions. Its well-defined redox behaviour, along with its high ion-exchange capacity and structural tunability, make it ideal for electrochemical sensing applications [15]. Furthermore, the addition of Mn to the hexacyanoferrate framework introduces new redox-active centres, which could help in the selective and sensitive detection of target analytes. These characteristics establish MnHCF as an effective and adaptable material for the construction of next-generation electrochemical sensors. On the other hand, Mn based PBAs have limited use in high-performance electrochemical sensing due to their inherent limitations, which includes weak mechanical stability and poor electrical conductivity. To address these restrictions, multiple efforts such as metal doping [16], making hybrids with conductive materials [17] have been made to produce various composites incorporating transition metal hexacyanoferrates (TMHCFs). Recently, hybrids of carbon-based materials and PBAs have been developed to capitalise on their combined benefits, addressing the increasing demand for electrochemical sensor electrode design [18]. Because of the synergistic interactions between the components, these hybrid materials consistently outperform pure TMHCFs in terms of electrochemical performance and stability.

Recently, heteroatom-doped carbon dots (CDs), particularly nitrogen and phosphorus co-doped CDs have drawn significant attention in the field of electrochemical sensing materials owing to its numerous advantages such as superior conductivity, rich surface functional groups and a high electron-donating ability [19]– [20]. The inclusion of N, P-doped CDs not only improves the electrical conductivity of MnHCF, but it also adds more active sites and improves surface interactions with analytes. This synergistic combination lays the path for the creation of a reliable and sensitive electrochemical sensor platform.

Several synthesis methods have been devised to make CDs, including top-down approaches such as laser ablation, arc discharge, and electrochemical oxidation, as well as bottom-up methods such as pyrolysis, hydrothermal, and microwave-assisted carbonisation of organic precursors [21]– [22]. While these technologies provide control over particle size and functionalisation, they frequently involve harsh chemicals, a large energy input, and complicated purification stages. To circumvent these restrictions, green synthesis techniques have received a lot of interest. These eco-friendly processes use renewable natural precursors including fruit extracts, plant leaves, and biomass waste in moderate circumstances, lowering environmental impact and production costs. For example, Wazir et al. (2013) described the synthesis of luminous CDs utilising orange juice in a one-step hydrothermal procedure, emphasising simplicity and biocompatibility [23]. Similarly, Sahu et al. (2022) created N doped CDs from banana peels, which showed strong fluorescence and good electrochemical characteristics appropriate for sensing applications [24]. Green synthesis not only adheres to sustainability principles, but it also naturally imparts heteroatom doping (e.g., N, P, S) from the precursors, hence improving the electrical and catalytic properties of CDs without the need for extra dopants. These inherent benefits make green-synthesized CDs especially appealing for integration with electroactive materials such as MnHCF in the construction of high-performance, environmentally friendly electrochemical sensors.

In this context, the rationale of the present work lies in combining the advantages of MnHCF with heteroatom-doped CQDs to overcome their respective shortcomings. While MnHCF contributes multiple reversible redox-active centers (Mn^{2+}/Mn^{3+} and Fe^{2+}/Fe^{3+}), its poor electrical conductivity and moderate mechanical stability limit its sensing efficiency. Incorporation of nitrogen and phosphorus co-doped CQDs addresses these limitations by offering superior conductivity, abundant functional groups (–OH, $–NH_2$, –COOH), and strong electron-donating capability. N-doping enhances electron transfer and active site density, while P-doping promotes surface reactivity and electron delocalization, enabling stronger electrostatic and π–π interactions with aromatic drug molecules such as Sneprin. Moreover, the use of orange peel as a sustainable precursor for NPCQD synthesis through a green hydrothermal route ensures cost-effectiveness and biowaste valorization, while simultaneously introducing natural heteroatom doping. Thus, the MnHCF/NPCQD hybrid electrode is strategically designed to integrate structural stability, enhanced conductivity, and eco-friendly fabrication, providing a robust platform for ultrasensitive and sustainable Sneprin detection.

2 Experimental Procedure

2.1 Materials

Fresh orange peels were collected from local sources and thoroughly cleaned with distilled water. Manganese (II) chloride tetrahydrate ($MnCl_2{\cdot}4\ H_2O$) (>99%), potassium ferricyanide (K_3 [Fe (CN)$_6$]) (>99%) were purchased from Sigma Aldrich chemicals and Co., Bangalore. Phosphoric acid (H_3PO_4) (>95%), urea (>98%) and glucose (>98%) was supplied by Merck Chemical Company, Chennai. Ethanol, hydrochloric acid, potassium chloride was provided by Naresh Scientific Company, Pudhucherry, India. Sneprin 75 mg tablet was purchased from local medical store, Chennai. All reagents were of analytical grade and used without further purification.

2.2 Synthesis of N, P-Doped Carbon Quantum Dots from Orange Peels

A green hydrothermal technique was used to synthesise N, P-doped carbon quantum dots from orange peels. In this procedure, initially, orange peels were cleaned, sliced into small pieces, and dried at 60 °C before being ground into powder. 1.0 g of orange peel powder was mixed with 30 mL of DI water containing 1.0 g of urea and 0.5 mL of phosphoric acid. The solution was agitated for 30 min and transferred to a 50-mL Teflon-lined stainless-steel autoclave. The autoclave was heated to 180 °C for 6 h for hydrothermal process. After naturally cooling to ambient temperature, the dark brown solution was centrifuged at 10,000 rpm for 15 min. The supernatant containing well-dispersed N, P-CQDs was kept at 4 °C, labelled as NPCQD and used for fabricate composite.

2.3 Synthesis of MnHCF and NPCQD/MnHCF Composite

The nanocomposite was produced by mixing 10 mL of the as-prepared N, P-CQD solution with 20 mL of 0.01 M $MnCl_2{\cdot}4\ H_2O$ solution while stirring constantly. Next, the mixture was mixed with 20 mL of 0.01 M $K_3[Fe(CN)_6]$ solution added dropwise. The development of the composite was shown by the slow production of a blue manganese hexacyanoferrate (MnHCF) precipitate. At room temperature, the reaction was stirred for 4 h. Centrifugation was used to gather the finished product, which was then periodically cleaned with ethanol and DI water to get rid of any unreacted species. It was then dried for 12 h at 60 °C in a vacuum oven. N, P-CQD/MnHCF nanocomposite was the label applied to the dried powder. A similar co-precipitation technique was used to synthesise pristine manganese hexacyanoferrate without adding N, P-CQDs [25]. In particular, 20 mL of 0.01 M $MnCl_2{\cdot}4\ H_2O$ and 20 mL of 0.01 M K_3[Fe (CN)$_6$] were combined for 4 h with constantly stirred. The blue precipitate that resulted was then collected, washed and dried at 60 °C. The formed composite and pristine sample were labelled as MnHCF/NPCQD and MnHCF respectively. The schematic representation of the synthesis of MnHCF/NPCQD nanocomposite is depicted in Fig. 1.

2.4 MnHCF/NPCQD Electrode Fabrication Procedure

The electrode fabrication using MnHCF/NPCQD structures was achieved by adapting a protocol reported in our previous work with slight modifications [26]. In this procedure, a glassy carbon electrode (GCE, diameter 3 mm) was chosen as the base working electrode for the electrochemical sensor fabrication. To attain a mirror-like finish, its surface was mechanically polished using alumina slurry (0.05 µm) on a polishing cloth in eight number writing motion. The electrode was then completely cleaned with ethanol and deionized water to get eliminate of any remaining fragments of alumina and surface contaminants. Subsequently, a mild N_2 gas stream was used to dry the cleaned GCE. A conducting binder consisting of ethanol and 5 wt% Nafion (480 µL ethanol + 20 µL Nafion) was used to produce a slurry of MnHCF/NPCQD nanocomposite in order to modify the GCE. The slurry was prepared by mixing an appropriate amount (5 mg) of the synthesised powder with the solution.

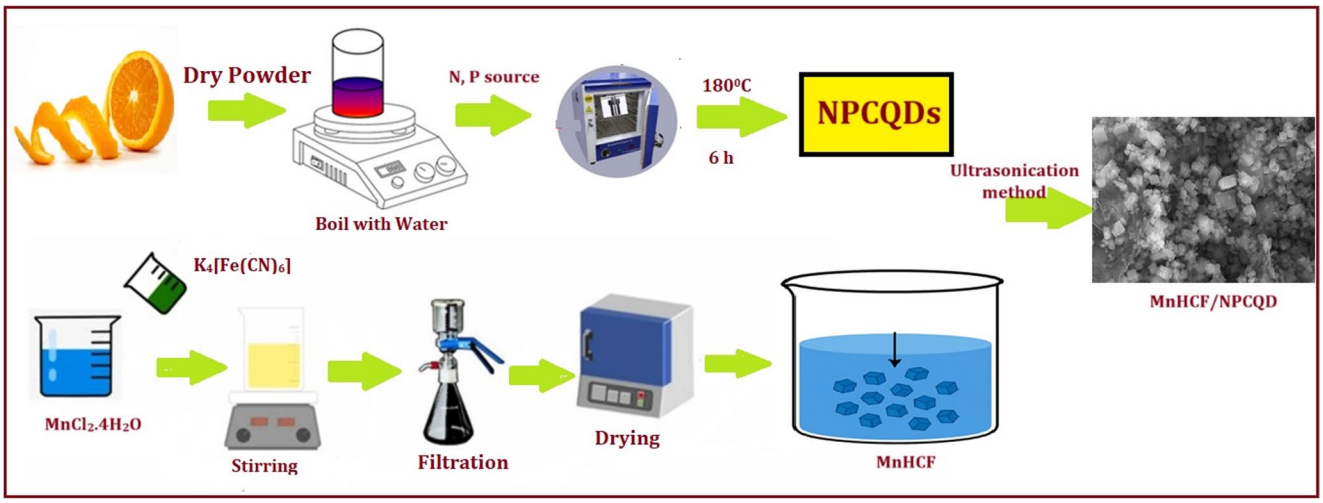

Fig. 1 Schematic illustration of synthesis of MnHCF/NPCQD

To form a homogeneous and stable slurry, the resulting mixture was ultrasonicated for 30 min. The slurry was subsequently drop-casted onto the surface of a GCE. The modified electrode was dried in an electric oven at 60 ± 5 °C for 5 h subsequent the coating process to ensure proper adhesion and film formation. The modified electrode is referred to as MnHCF/NPCQD/GCE and it was used for electrochemical detection of sneprin.

2.5 Characterization

Using a Bruker D8 Advance diffractometer with Cu Kα radiation (λ = 1.5406 Å) running at 40 kV and 40 mA over a 2θ range of 10°–80°, the crystalline nature of the samples was investigated by X-ray diffraction (XRD). To determine the functional groups included in the samples, FTIR spectra were captured using a Shimadzu IRTracer-100 spectrometer in the 4000–400 cm^{-1} range. Field emission scanning electron microscopy (FESEM, ZEISS Sigma 300) combined with an energy-dispersive X-ray spectroscopy (EDS) equipment was used to examine the surface morphology and elemental distribution. A JEOL JEM-2100 microscope running at an accelerating voltage of 200 kV was used to acquire transmission electron microscopy (TEM) and high-resolution TEM (HRTEM) images in order to examine the internal morphology and particle distribution at the nanoscale. To ascertain the elemental composition and chemical states of the elements in the nanocomposite, X-ray photoelectron spectroscopy (XPS) investigation was performed using a Thermo Scientific K-Alpha + spectrometer with Al Kα radiation (hv = 1486.6 eV).

3 Results and Discussion

3.1 Powder XRD Analysis

Powder XRD pattern of MnHCF/NPCQD is presented in Fig. 2. The appeared diffraction peaks at 2θ = 17.4°, 24.7°, 35.1°, 39.4° and 43.2° correspond to the (200), (220), (400), (420) and (422) planes of face-centered cubic MnHCF. These peaks closely resemble the standard pattern of JCPDS Card No. 89–0686 and are consistent with earlier literature [27]. The presence of nitrogen and phosphorus co-doped carbon quantum dots (NPCQDs) in the nanocomposite is confirmed by the broad feature observed around 24°, which is indicative of the (002) plane of graphitic carbon [28]. This broadening indicates a partially disordered carbon structure that is typical of carbon quantum dots that are synthesised from biomass precursors of orange peels. The XRD spectrum shows no additional impurity peaks, confirming the phase purity of the synthesised composite. Beyond phase identification, the XRD data were used to extract quantitative structural parameters for the MnHCF/NPCQD composite. The crystallite size (D) was estimated using the Debye–Scherrer formula [29]:

$$D = \frac{0.9\lambda}{\beta\, cos\theta}$$

with Cu Kα radiation (λ = 1.5406 Å), giving D ≈ 36.0 nm (consistent with our earlier estimate from the (220) reflection). The microstrain (ε) was obtained from peak broadening by using following equation:

$$\epsilon = \frac{\beta}{4tan\theta}$$

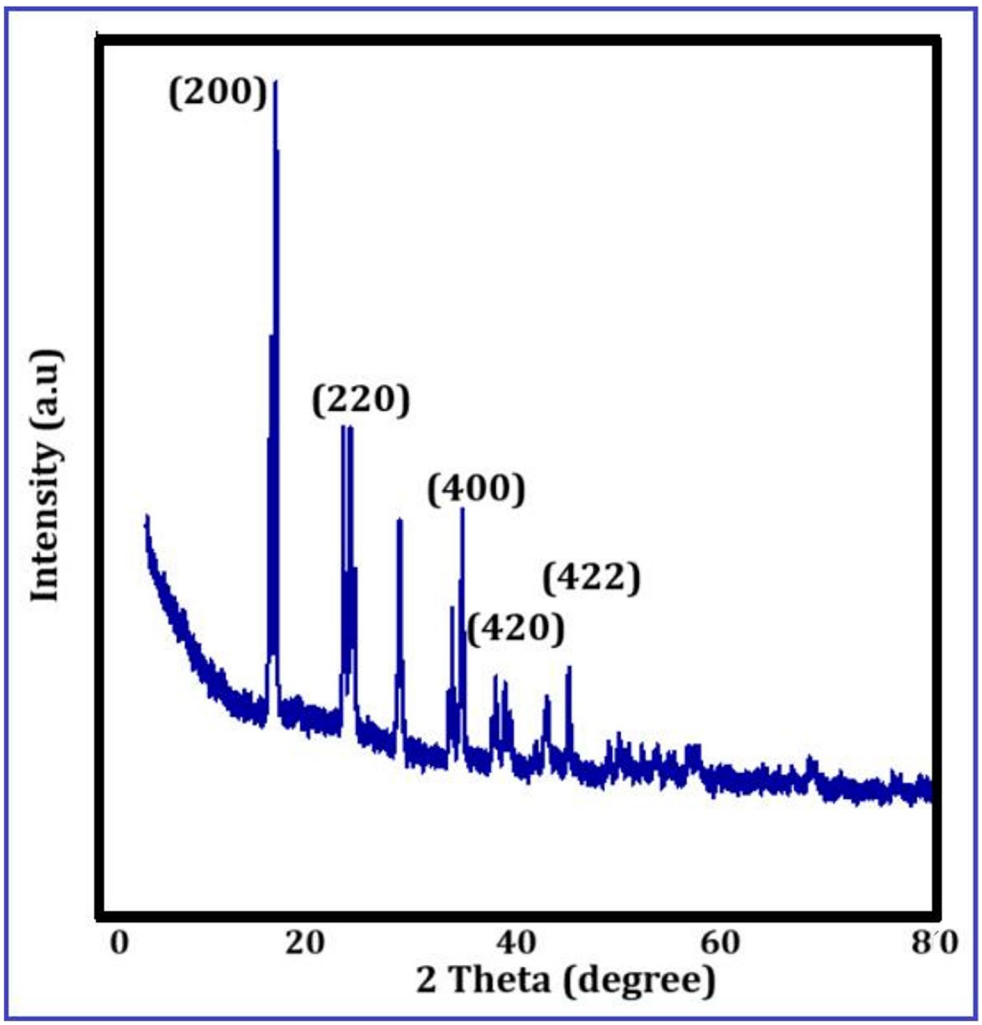

Fig. 2 XRD pattern of MnHCF/NPCQD

yielding $\varepsilon \approx 2.8 \times 10^{-3}$ and the corresponding dislocation density (δ) is $\delta \approx 0.77 \times 10^{15} m^{-2}$. These values signify excellent crystallinity accompanied with a minimal density of lattice flaws. The lattice constant (a) for MnHCF was determined from multiple indexed peaks, assuming a cubic lattice structure. Utilising the reflections at $2\theta = 17.4°$ (200), 24.7° (220), 35.1° (400), 39.4° (420), and 43.2° (422), the individual values converge to an average of $a = 10.20 \pm 0.03$ Å, consistent with the documented cubic PBA framework [30]. To evaluate the degree of crystallinity (Xc), we integrated the areas of the crystalline peaks and normalized to the total diffracted area (peaks + background), explicitly accounting for the broad amorphous contribution centered near ~ 24° associated with the CQD component. This gives Xc ≈ 72% for MnHCF/NPCQD. As XRD is not a direct porosimetry method, we report a qualitative XRD-derived porosity index as the complementary amorphous fraction: $P_{XRD}=1 - Xc \approx 28\%$. Based on this, the composite exhibits a moderate crystallite size (~ 36 nm), low microstrain, and a well-defined cubic lattice (a ≈ 10.20 Å) with a high crystalline fraction (~ 72%), which together rationalize the stable redox features and efficient charge transfer observed in the electrochemical studies.

3.2 FTIR Analysis

FTIR spectra of MnHCF/NPCQD is presented in Fig. 3. A strong and distinct absorption peak appeared near 2075 cm^{-3}. This is due to the cyanide group's stretching vibration, which is an important part of manganese hexacyanoferrate (MnHCF)'s structure [31]. The presence of this peak confirms the formation and structural integrity of the Mn–CN–Fe framework. Moreover, the intense peak at appeared at approximately 1625 cm^{-1} corresponds to the bending vibration of adsorbed H–O–H from surface-bound water or hydroxyl groups, whereas the peak at 1395 cm^{-1} is likely attributed to C–N stretching vibrations from doped nitrogen groups within the NPCQDs [32]. The presence of -OH and $-NH_2$ functional groups introduced during the synthesis of carbon dots from the orange peel precursor is indicated by

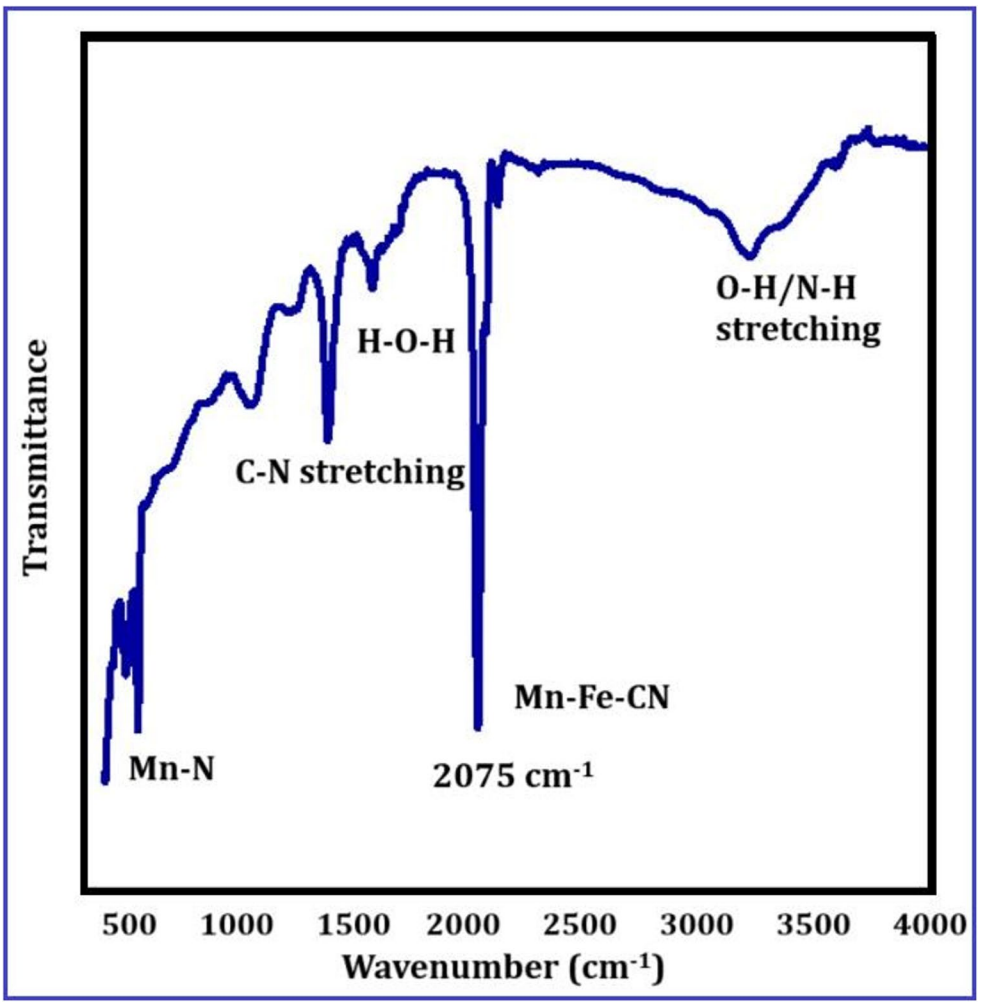

Fig. 3 FTIR spectra of MnHCF/NPCQD

the broad band centred around 3410 cm^{-1}, which is characteristic of O–H/N–H stretching vibrations. In the lower wavenumber range, bands at around 580 cm^{-1} and 480 cm^{-1} correspond to Mn–N and Fe–C stretching modes, thereby affirming the coordination environment within the Prussian blue analogue structure [33]. The combination of cyanide stretching, metal-ligand vibrations, and surface functional group bands confirms the effective fabricating of the MnHCF/NPCQD composite, as well as the inclusion of surface-active groups from carbon dots, which are critical for improving electrochemical sensing characteristics.

3.3 FESEM Analysis

The FESEM micrographs at different magnifications are presented in Fig. 4 (a–c). As shown in Fig. 4 (a) (at a 2 µm scale), the nanocomposite exhibits a porous texture and a densely aggregated morphology with interconnected particles. Figure 4 (b) (at a 1 µm scale) illustrates a more pronounced distribution of nearly cubic particles, which is indicative of the crystalline character of the MnHCF phase. The MnHCF framework and NPCQDs are believed to form a significant interaction, as these structures are uniformly distributed throughout the carbonaceous matrix. The particles exhibit well-defined edges and slightly rough surfaces at a higher magnification in Fig. 4 (c). The irregularity may be attributed to the deposition of NPCQDs on the MnHCF surfaces, which produces a hybrid nanostructure. The dense arrangement and the absence of large voids further support effective surface coverage, which is advantageous for improved charge transport during sensing. Figure 4 (d) illustrates that the main elements are uniformly distributed across the MnHCF/NPCQD composite. The detection of Fe, Mn, K, N, P, and O validates the synthesis of MnHCF and the effective incorporation of N and P into the carbon quantum dots derived from orange peel biomass. The homogeneous distribution of nitrogen and phosphorus signifies efficient doping of N and P in biomass derived carbon dot, which enhances electrochemical conductivity and surface activity. The elemental composition is further confirmed by the EDX spectrum, which is displayed in Fig. 4 (e). The presence of distinctive peaks for Fe, Mn, K, O, N and P

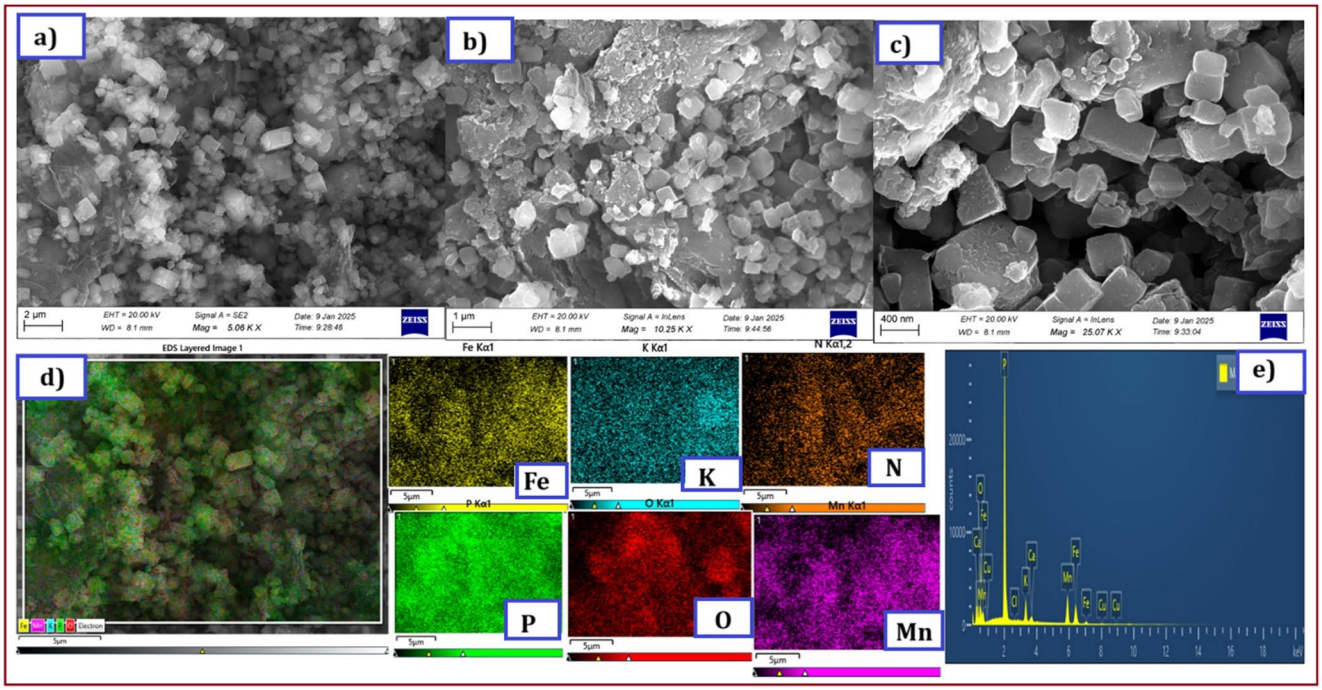

Fig. 4 FESEM images of MnHCF/NPCQD at various magnifications (**a**) at 2 µm (**b**) at 1 µm (**c**) at 400 nm (**d**) Elemental mapping (**e**) EDS spectra of MnHCF/NPCQD

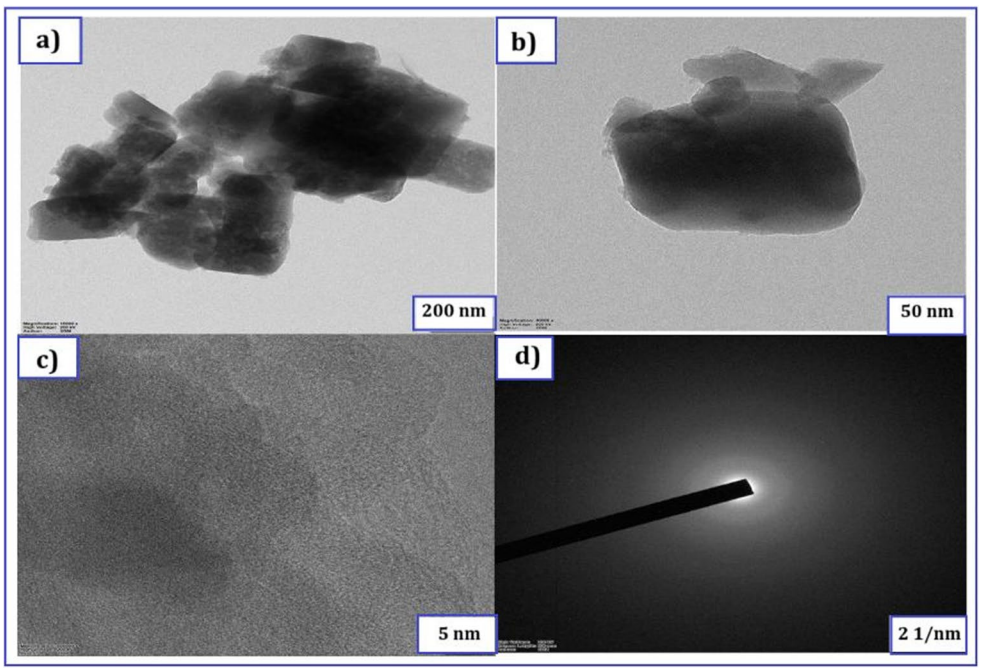

Fig. 5 TEM images of MnHCF/NPCQD at various magnification (**a**) at 200 nm (**b**) at 50 nm

validates the integration of the doped CQDs with the hexacyanoferrate framework.

3.4 TEM Analysis

In order to acquire a more comprehensive understanding of the morphology and nanostructure of the MnHCF/NPCQD composite, transmission electron microscopy was used. Figure 5(a) illustrates the low-magnification TEM image (200 nm scale), which clearly demonstrates aggregated polyhedral particles. These particles exhibit moderate aggregation and are indicative of the MnHCF crystalline structure, which may be attributed to the interaction between the particles and the carbon matrix. Figure 5(b) (50 nm

scale) illustrates the way the surface morphology of individual particles becomes increasingly visible at higher magnifications. A slightly even coating or shell-like contrast is detected surrounding the MnHCF particles, indicating the presence of NPCQDs anchored to or partially encircling the surface of the MnHCF crystallites. Furthermore, the clear lattice fringes with interplanar distances of approximately 0.25–0.32 nm were measured in HRTEM image depicted in 5 (c), which correspond well to the characteristic planes of MnHCF.

Moreover, Fig. 5(d) shows a selected area electron diffraction (SAED) pattern with clear concentric diffraction rings. The mix of narrow and wide rings supports the existence of both crystalline MnHCF domains and the amorphous or partially crystalline carbon structure formed by the NPCQDs.

3.5 XPS Analysis

Figure 6(a) shows the XPS survey spectrum of the MnHCF/NPCQD nanocomposite. The presence of Fe, Mn, O, C, N, P and K elements is clearly indicated by sharp peaks which validates the successful formation of the composite structure comprising MnHCF and N, P-doped carbon quantum dots. The high-resolution Fe 2p spectrum is displayed in Fig. 6(b), with two distinct peaks at around 708.5 eV and 722.3 eV, which correspond to Fe 2p$_{3/2}$ and Fe 2p$_{1/2}$, respectively [34]. The presence of Fe^{2+} species in the MnHCF framework is confirmed by these peaks, which is in accordance with literature reports on Prussian blue analogues. In addition, the existence of Mn^{2+} in the composite is confirmed by Fig. 6 (c), which displays Mn 2p peaks at approximately 641.8 eV and 653.4 eV, which correspond to Mn 2p$_{3/2}$ and Mn 2p$_{1/2}$ [35]. Furthermore, the core level C 1 s spectrum has a primary peak about 284.8 eV, which is attributed to C-C/C = C bonds, as well as smaller features near 286.2 eV and 288.5 eV, which correspond to C-O and O-C = O functional groups, respectively (Fig. 6(d)) [36]. Figure 6(e) illustrates the N 1 s peak centred at approximately 398.3 eV, indicative of pyridinic nitrogen, accompanied by a shoulder near 400.5 eV, which corresponds to graphitic or doped nitrogen within the NPCQD matrix [37]. Moreover, P 2p spectrum with a peak at about 133.8 demonstrating that P in its oxidised state has been successfully incorporated into the carbon matrix (Fig. 6 (f)). The strong O 1 s peak centered at ~ 532.1 eV, which can be attributed to oxygen in metal–oxygen bonds and surface-adsorbed hydroxyl or carbonyl groups (Fig. 6(g)) [38]. The XPS investigation indicates that the MnHCF/NPCQD composite has all of the required elements, including Mn, Fe, C, N, P, and O, indicating that the material was successfully synthesised with the desired composition.

3.6 CV Analysis for Detection of Sneprin by MnHCF/NPCQD/GCE

The electrochemical sensing capacity of the MnHCF/NPCQD-modified GCE towards sneprin was systematically examined using CV in a 0.1 M KCl electrolyte within the potential window from − 1.0 V to 1.0 V at a scan rate of 50

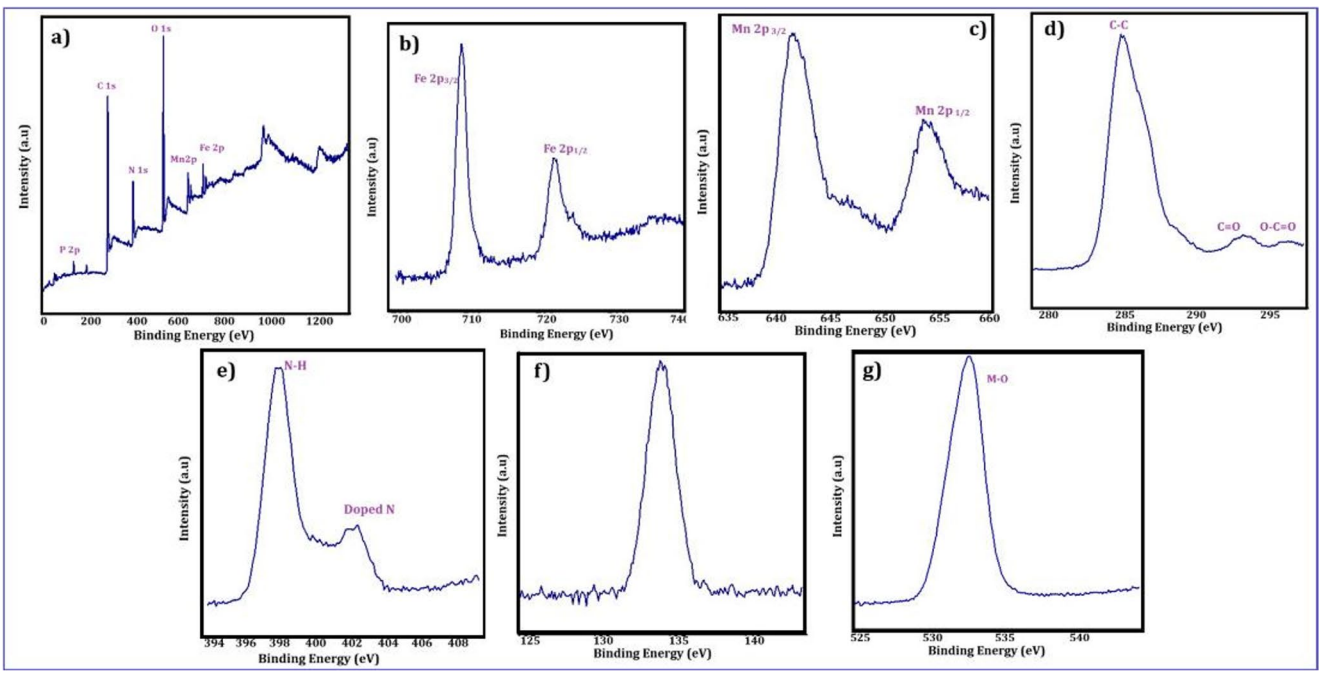

Fig. 6 XPS spectra of MnHCF/NPCQD (**a**) XPS survey spectrum; High resolution spectra (**b**) Fe 2p (**c**) Mn 2p (**d**) C 1 s (**e**) N 1 s (**f**) P 2p (**g**) O 1s

mV s^{-1}. The bare GCE's performance was initially assessed and the obtained results demonstrated that bare GCE exhibited very weak redox activity with negligible peak currents in the presence of sneprin due to its limited surface area and lack of electrocatalytic properties. However, the electrochemical response was significantly improved after modification with the MnHCF/NPCQD nanocomposite. This was attributed to the synergistic combination of redox-active MnHCF and highly conductive N and P co-doped carbon quantum dots. The MnHCF provides reversible redox couplings (Mn^{2+}/Mn^{3+} and Fe^{2+}/Fe^{3+}), whereas NPCQDs enhance surface area, conductivity, and electrostatic and π-π interactions with sneprin molecules [39]. To investigate the sensing behaviour under different concentration regimes, CV measurements were carried out with gradually increasing amounts of sneprin from 10 µL to 2000 µL. We evaluated sneprin concentrations ranging from 100 to 1900 µL in Fig. 7 (a), 10 to 100 µL in Fig. 7(b) and 100 to 1000 µL in Fig. 7 (c). In all cases, increasing sneprin concentration resulted in a gradual increase in both anodic and cathodic peak currents indicating the improved electrochemical oxidation/reduction behaviour. The modified electrode exhibited a pair of well-defined redox peaks, corresponding to the Mn (II)/Mn (III) and Fe (II)/Fe (III) transitions inside the MnHCF framework. The addition of sneprin resulted in a progressive increase in both anodic and cathodic peak currents, with no significant changes in peak potential. This signifies a strong and stable electrochemical contact between sneprin molecules and the electrode surface.

To assess electrode sensitivity, calibration plots have been made by plotting anodic peak current (Ipa) against sneprin concentration (C) (Fig. 8 (a-c)). The relationship was determined to be linear across each examined range, and the sensitivity (S) of the electrode was computed utilizing the conventional linear regression formula [40]:

$$S = \frac{\Delta I}{\Delta C}$$

where, I is the peak current (mA), C is the analyte concentration (µL) and m is the slope of the line, representing the sensitivity. The calculated sensitivities are 0.00085 mA/µL, 0.00642 mA/µL and 0.00145 mA/µL for each range of concentrations.

These results validate that the sensor operates perfectly in both low and moderate concentration ranges, exhibiting a constant electrochemical response. Among the evaluated ranges, Fig. 6(b) exhibited the greatest sensitivity, which is

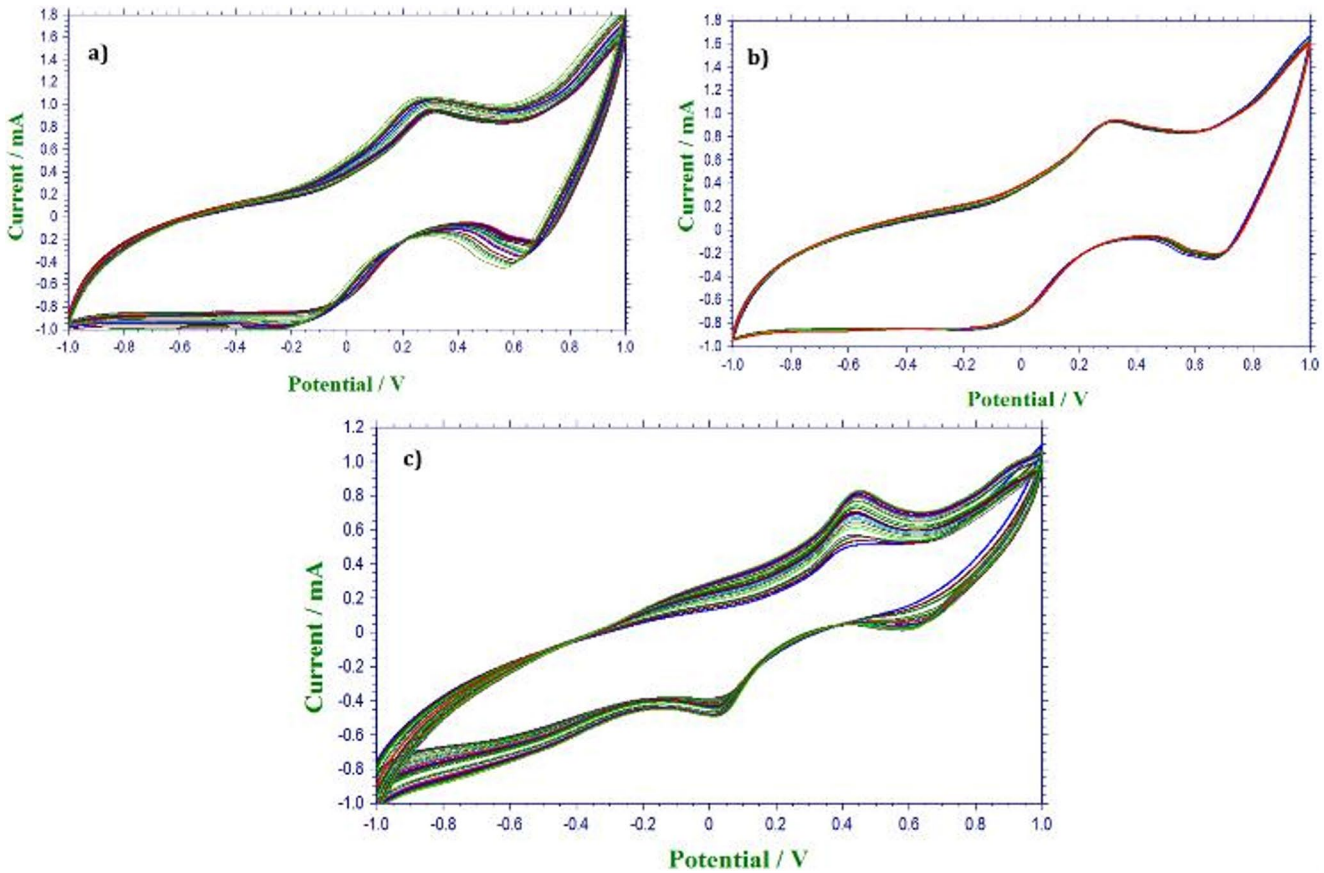

Fig. 7 CV curves of MnHCF/NPCQD electrode with varying sneprin concentrations (**a**) 100 to 1900 µL (**b**) 10–100 µL (**c**) 100–1000 µL

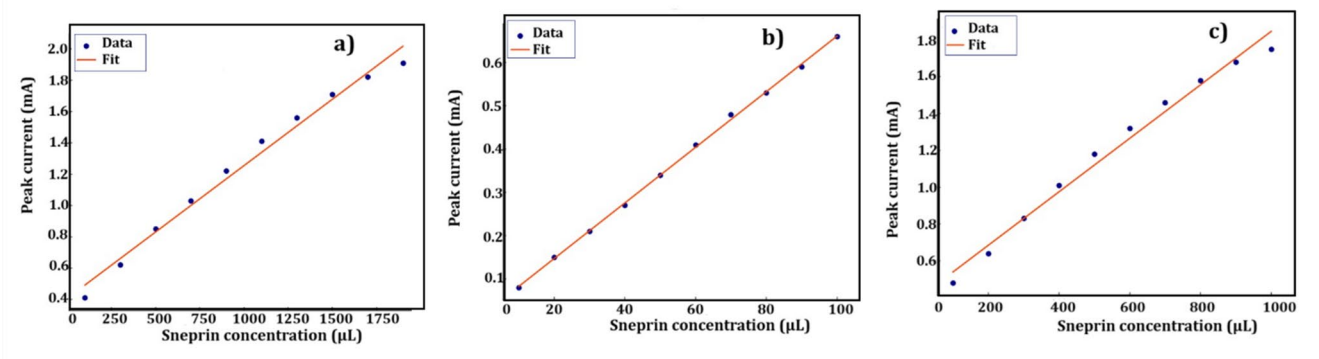

Fig. 8 Calibration plots of anodic peak current (Ipa) versus sneprin concentration (**a**) 100 to 1900 µL (**b**) 10–100 µL (**c**) 100–1000 µL

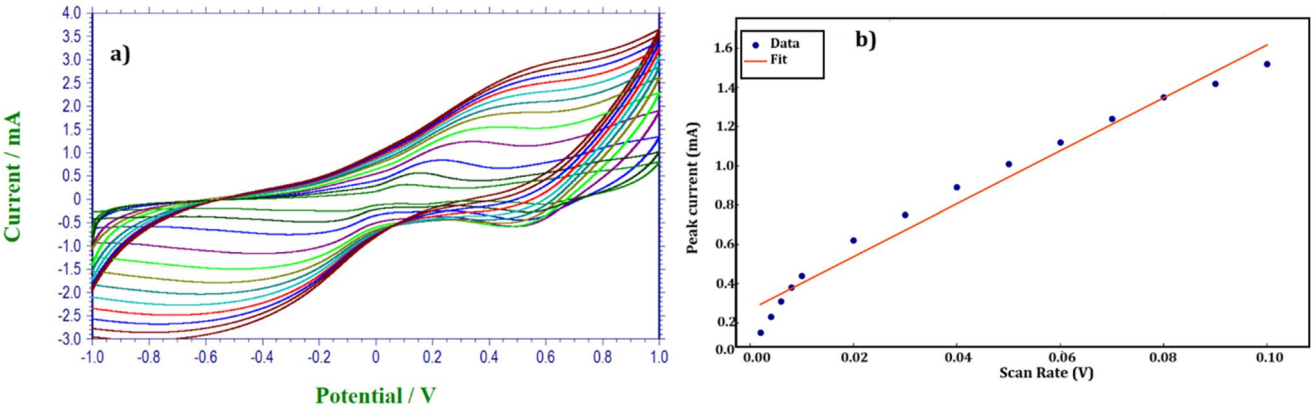

Fig. 9 (**a**) CV curves at different scan rates showing increasing redox current (**b**) Linear plot of Ipa versus scan rate

especially beneficial for detecting sneprin at trace concentrations. The elevated slope in this range signifies a robust interaction between sneprin and the plentiful surface-active sites at low coverage, where adsorption occurs. Moreover, CV measurements were conducted at scan rates from 2 mV s^{-1} to 100 mV s^{-1} in 0.1 M KCl with 1 mM sneprin to elucidate the electrochemical kinetics and charge transfer mechanism of the MnHCF/NPCQD-modified electrode. Figure 9 (a) shows the recorded CV spectra at different scan rate which illustrates that both anodic and cathodic peak currents exhibited a progressive increase with the elevation of the scan rate. The peak potentials displayed negligible shift, signifying a steady and quasi-reversible redox process at the electrode surface. To further understand the reaction process, a plot of anodic peak current (Ipa) versus scan rate (v) was generated. The resulting linear connection (Fig. 9(b)) demonstrates that the electrochemical response is predominantly determined by a surface-controlled process in which the current is directly proportional to the scan rate [41].

This shows that sneprin's redox behaviour at the MnHCF/NPCQD interface is determined by adsorption rather than diffusion-limited transport across the electrolyte. The sensor's sensitivity to scan rate was evaluated using linear regression of the Ipa vs. ν plot, based on the following equation [42]:

$$I_{pa} = kv + b$$

where $_{p.a.}$ is the anodic peak current (mA), is the scan rate (mV/s), is the slope of the linear fit and is the intercept. The sensitivity of the electrode in response to scan rate variation is represented by the slope of this plot, which was determined to be 13.49 mA V^{-1} s^{-1}. The MnHCF/NPCQD composite's superior electron transfer capability and high electroactive surface area are evidenced by this high value. The synergistic interaction between the conductive, functionalised surface of NPCQDs and the redox-active MnHCF framework is responsible for the improved response. During redox transitions, the efficient transportation of electrons is facilitated by the abundant nitrogen and phosphorus surface functionalities and the porous morphology, which provides sneprin molecules with ample anchoring sites [43]. These results not only substantiate the sensor's rapid charge transfer kinetics but also confirm its suitability for real-time electrochemical sensing applications.

3.7 DPV Analysis for Detection of Sneprin by MnHCF/NPCQD/GCE

To determine the electrode's limit of detection and suitability for low-concentration sensing, differential pulse voltammetry (DPV) analysis is more important study, which was performed in 0.1 M KCl electrolyte with a progressive injection of sneprin from 10 µL to 200 µL. As shown in Fig. 10(a), DPV curves show a distinct oxidation peak with a steady and progressive rise in peak current as the concentration of sneprin increases. The MnHCF/NPCQD-modified electrode showed a markedly improved response under the same conditions as the bare MnHCF electrode, which showed a peak current of 105.4 µA at 10 µL of sneprin. The increased electroactive surface area and better electron transfer kinetics brought forth by the NPCQDs are responsible for this improvement. These doped locations provide advantageous functional groups that improve interaction with sneprin molecules in addition to increasing conductivity [44]. The linear calibration plot (Fig. 10(b)) shows the quantitative evaluation of the sensor's sensitivity by graphing the peak current (Ipa) against the sneprin concentration (C). According to the regression equation, there was a linear relationship:

$$I = 1.37 \times C = 127.64$$

where I is the peak current in µA and C is the sneprin concentration in µL. The slope of this line correlates to the sensitivity, which is computed to be 1.37 µA/µL. This shows a strong and linear current response in the tested range. This linearity verifies the MnHCF/NPCQD-modified electrode's outstanding performance in quantitative analysis. The limit of detection (LOD) of the MnHCF/NPCQD sensor was further estimated using the standard formula [45]:

$$LOD = \frac{3.3 \times \sigma}{S}$$

where the standard deviation of the blank () is assumed to be 1.5 µA, and the sensitivity () is derived from the calibration curve (1.37 µA/µL). The developed electrode had an exceptional low-level detection capability, as evidenced by the calculated LOD of approximately 3.63 µL. The MnHCF/NPCQD nanocomposite is a highly sensitive platform that is suitable for trace-level quantification of sneprin in environmental or clinical contexts, as evidenced by the low LOD value.

3.8 Electrochemical Impedance Spectroscopy (EIS) Analysis

The interfacial charge transfer characteristics of the MnHCF/NPCQD-modified electrode were examined before and after the addition of sneprin using electrochemical impedance spectroscopy (EIS). The Bode diagrams in Fig. 11(a) and Fig. 11 (b) illustrate the logarithmic scale variation of impedance magnitude (|Z|) and phase angle in relation to frequency. The system exhibited a total impedance value of approximately 138.3 Ω at 1 Hz and a phase angle of 8.3° in the absence of sneprin (Fig. 11(a)). The phase angle was slightly reduced to 7.5°, and the impedance was marginally reduced to 135.1 Ω after 1 mL of sneprin was added to the electrolyte (Fig. 11(b)). The minimal decrease in both |Z| and phase angle suggests a modest enhancement in charge transfer dynamics at the electrode–electrolyte interface

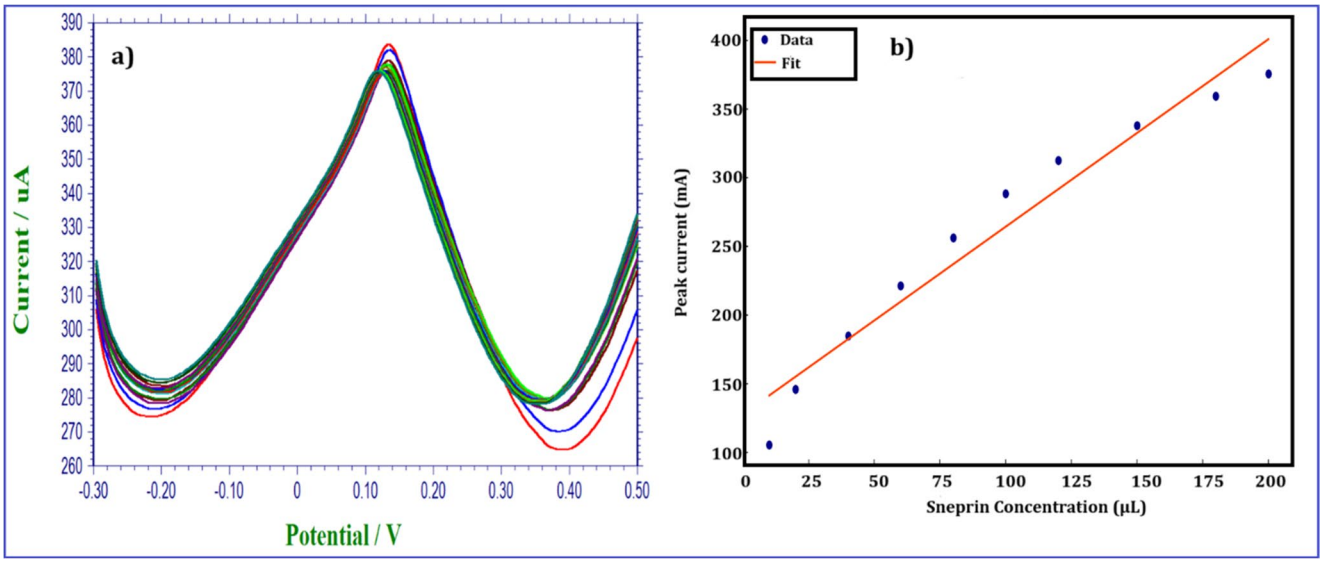

Fig. 10 (**a**) DPV curves of MnHCF/NPCQD electrode with increasing sneprin concentrations (**b**) Corresponding calibration plot used to determine sensitivity and LOD

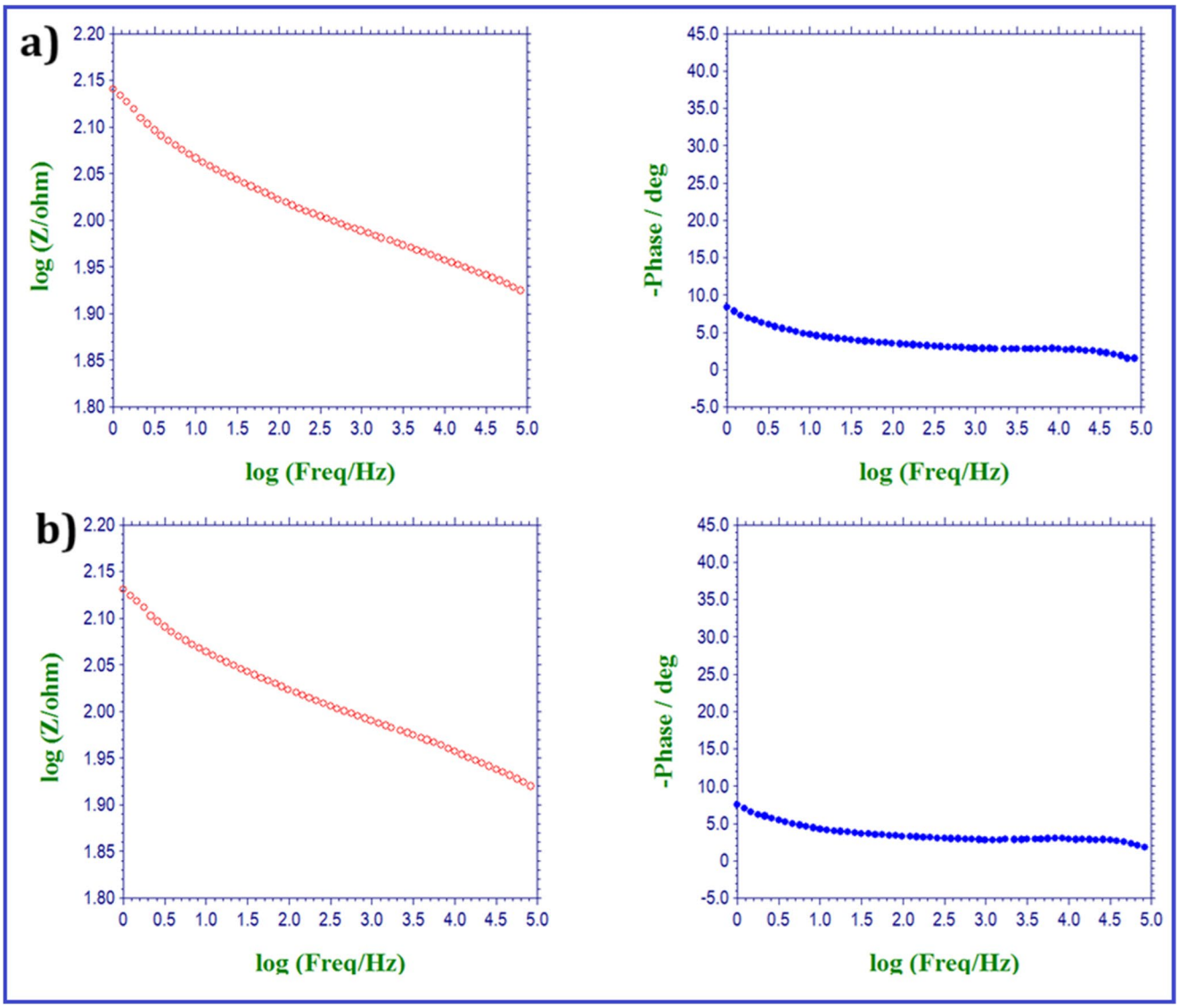

Fig. 11 (**a**) Bode plot of impedance magnitude and phase before sneprin addition (**b**) Bode plot after sneprin addition

as a result of sneprin binding [46]. The increased electrochemical activity observed in the CV and DPV results is consistent with the decrease in impedance that occurs upon analyte introduction. It implies that the presence of sneprin facilitates the electrostatic and chemical interaction between sneprin molecules and the functional sites of the MnHCF/NPCQD surface, thereby promoting quicker electron transfer. In order to facilitate efficient redox exchange, the N and P dopants in the CQDs may contribute additional conductivity and anchoring sites.

3.9 Stability Analysis and Comparison with Earlier Reports

The electrochemical response of the MnHCF/NPCQD-modified electrode was monitored for 30 days under ambient storage conditions in order to assess its long-term operational stability. Multiple electrochemical cycles were used for stability experiments in order to evaluate the MnHCF/NPCQD-based sensor's practical reliability. Excellent repeatability was demonstrated by the electrode's current response, which stayed constant with very little change in peak intensity. After 30 days, the sensor maintained roughly 93.8% of its initial current response, as illustrated in Fig. 12(a), demonstrating exceptional stability and resilience. On Day 1, the electrode first showed a 100% peak current. The percentage of responses that were kept after 5, 10, 15, 20, and 25 days were 98.7%, 97.5%, 96.8%, 95.9%, and 94.6%, respectively. The comparatively moderate rate at which the current decreases indicates that there is no appreciable loss of structural or redox integrity over time, and the electrode surface continues to be electrochemically active. The robust

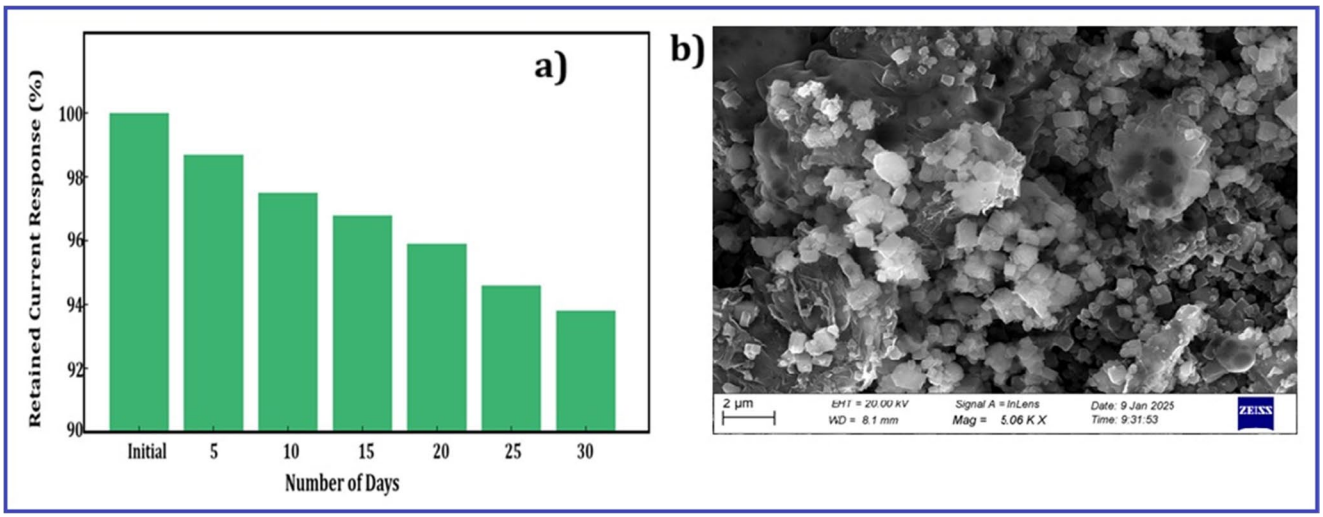

Fig. 12 (**a**) Stability analysis of MnHCF/NPCQD-modified electrode monitored over 30 days (**b**) Post SEM analysis image of MnHCF/NPCQD

Table 1 Comparison results of present work with previously published work towards electrochemical detection for pharmaceutical or NSAID detection

Sensor Material	Analyte	Detection limit	Sensitivity	Linear Range	Reference
Graphene modified SPE	Aspirin	8.7 µM	7.129 µA μM^{-1}	10–150 µM	[48]
Polythiophene	Aspirin	0.5–10 mM	20.62 $\mu A m M^{-1}$	100–1000 µM	[3]
Chitosan capped gold nanoparticle	Aspirin	0.03 pg/mL	-	1 pg/mL- 1 µg/mL	[49]
Polypyrrole/SiO_2@Au	Acetyl salicylic acid	0.2 nM	0.5214 µA/nM	10 nM −1000 nM	[50]
CNTs-ferrocene/nickel chromium oxide nanocomposite	Acetyl salicylic acid	1.26 nM	3.5×10^{-7} mol/L	0.01 µM-50 µM	[47]
MWCNTs-poly-4-vinylpyridine composite	Aspirin	4.42 nM	2.1×10^{-6} mol/L	0.04–350 µM	[51]
PMR/Zn-Al LDH/GCE	Acetyl salicylic acid	1.27 µM	43.3 µA μM^{-1}	0.1 µM to 4.25 µM	[52]
NPCQD/MnHCF	Sneprin	3.63 µL	0.00642 mA/µL	1 µM to 3000 µM	This work

interface between MnHCF and the co-doped carbon quantum dots, which successfully inhibit surface deterioration and improve durability, is responsible for the structural and electrochemical stability. Additionally, the CQDs' dopants of phosphorus and nitrogen help to sustain conductivity and electron transfer efficiency over time. These results validate the durability and reproducibility of the sensor, which makes it appropriate for long-term sneprin electrochemical monitoring [47].

Moreover, the MnHCF/NPCQD sensor was evaluated in comparison to sensors that had been previously reported for the detection of pharmaceuticals and NSAIDs. The present sensor provides a broader linear range, a lower limit of detection (LOD ≈ 3.63 µL) and comparable or superior sensitivity, as summarised in Table 1 [48–52]. The green synthesis route, which employs orange peel and low-cost precursors, is highly sustainable and cost-effective, in contrast to the fact that many sensors require complex synthesis procedures or pricey noble metals. To further confirm the structural stability of the MnHCF/NPCQD nanocomposite after extended electrochemical testing, post-characterization using SEM was performed on the electrode surface after 30 days of repeated measurements. As shown in Fig. 12 (b), the post-SEM image reveals that the nanocomposite maintained its interconnected polyhedral morphology, with MnHCF crystallites still embedded within the carbonaceous matrix of NPCQDs. No significant agglomeration, phase collapse, or film detachment was detected, indicating that the hybrid interface between MnHCF and NPCQDs is structurally robust. The retention of morphology strongly supports the electrochemical stability results, where ~ 93.8% of the initial current response was preserved even after 30 days. The combined electrochemical and post-morphological analyses confirm that the MnHCF/NPCQD nanocomposite is both durable and reliable for practical sneprin detection applications.

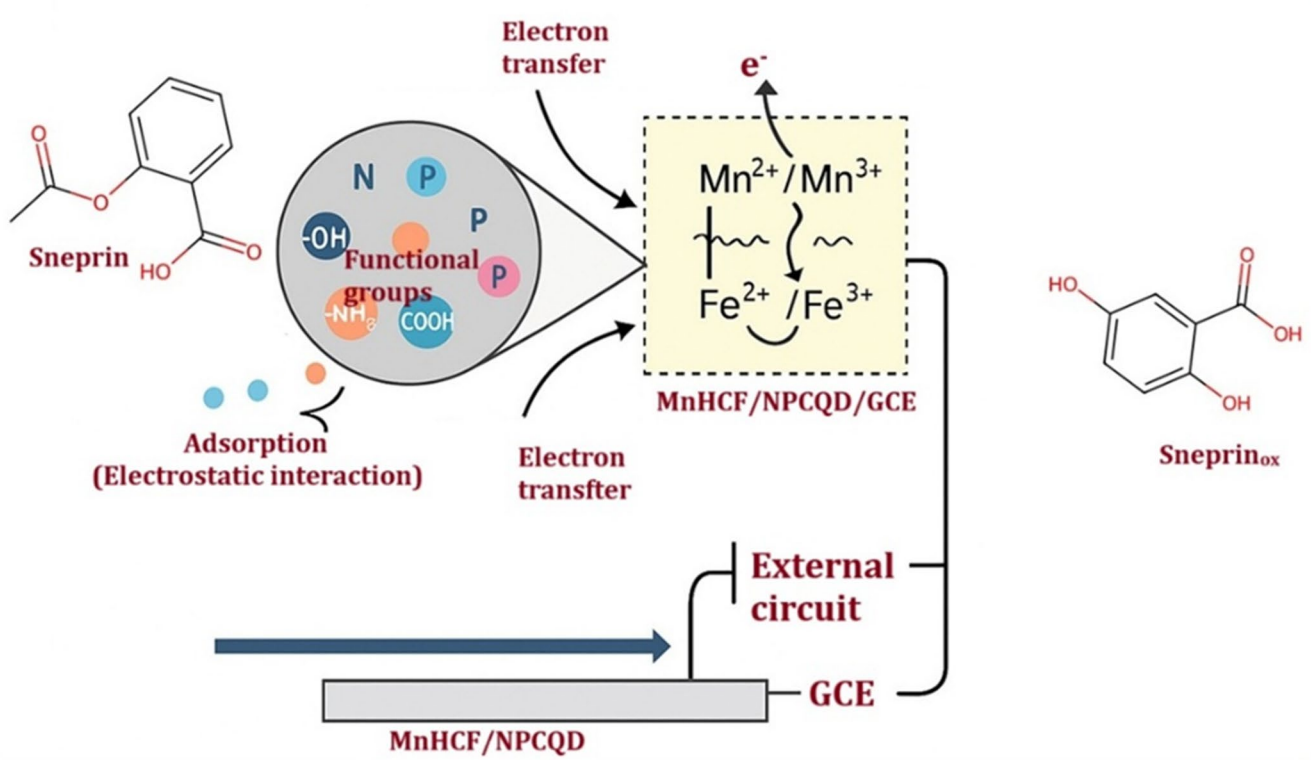

Fig. 13 Mechanism of enhanced sneprin detection of MnHCF/NPCQD

3.10 Mechanism

The mechanism of enhanced sneprin detection of MnHCF/NPCQD is schematically illustrated in Fig. 13. As illustrated, MnHCFs offers several redox-active centers such as Mn^{2+}/Mn^{3+} and Fe^{2+}/Fe^{3+} pairs which are enable effective electron transfer processes. The composite, when combined with NPCQDs exhibits increased surface area, enriched functional groups such as –OH, $–NH_2$, –COOH and higher electrical conductivity. Upon exposure to sneprin, which comprises aromatic and acidic functional groups, robust electrostatic interactions and π–π stacking transpire between the analyte and the surface of the NPCQDs [53]. These interactions facilitate the adsorption of sneprin onto the electrode surface, resulting in enhanced redox kinetics at the interface. The NPCQDs function as conductive conduits that transfer electrons between the sneprin molecules and the redox centres of MnHCF, leading to a significant enhancement in oxidation current detected in both CV and DPV results [54]. This mechanism is further supported by the electrochemical impedance spectroscopy results, which revealed a decrease in charge transfer resistance (Rct) upon the introduction of sneprin, confirming faster interfacial electron transfer. The surface-controlled behaviour observed in the scan rate study and the high sensitivity reported from DPV further validate this adsorption-driven electrocatalytic mechanism. MnHCF/NPCQD nanohybrid functions as a dual-active material, where MnHCF provides robust and reversible redox behaviour, while NPCQDs enhance electron transport and analyte binding. Therefore, the enhanced electrochemical sensing behaviour of the MnHCF/NPCQD-modified electrode towards sneprin arises from a synergistic interplay between the structural, electronic and surface-active characteristics of the hybrid nanocomposite. This cooperative mechanism enables rapid, selective, and sensitive detection of sneprin.

4 Conclusions

This study effectively synthesised and used a green biowaste-derived MnHCF/NPCQD nanocomposite as an electrochemical sensor for ultrasensitive sneprin detection. The formation of a crystalline MnHCF framework integrated with uniformly distributed, heteroatom-rich NPCQDs was confirmed by structural and morphological characterisations. The synergistic integration of MnHCF and NPCQDs provided the electrode with enhanced conductivity, multiple active sites, and consistent redox behaviour. Electrochemical analyses (CV, DPV, EIS) revealed remarkable sensitivity (1.37 µA/µL), a minimal detection limit (3.63 µL), and substantial stability (93.8% retention after 30 days). The design

technique presented—combining Prussian blue analogues with biomass-derived heteroatom-doped carbon quantum dots—provides a sustainable and scalable approach for advancing next-generation electrochemical platforms. This methodology can be expanded to selectively test additional non-steroidal anti-inflammatory medications (NSAIDs) and pharmaceutical pollutants in both clinical and environmental samples, beyond sneprin detection. Furthermore, the stability and environmentally benign synthesis method indicate its possible use in the production of portable, cost-effective sensor systems for on-site diagnostics. Future work may focus on miniaturization, integration into wearable or point-of-care devices, and real-sample validation in complex biological fluids and wastewater.Thus, the present work not only addresses a pressing need for sneprin monitoring but also provides a versatile blueprint for sustainable sensor design bridging green chemistry, nanotechnology, and environmental healthcare applications.

Acknowledgements The authors express their deep gratitude to the Central Instrumentation Laboratory at Vels University (VISTAS) for their comprehensive support throughout this research. Special thanks are extended to Sathyabama University, Chennai, for providing SEM, XPS characterization, SRM University, Kattankulathur for TEM characterization. We are particularly thankful to Dr. B. Muthuraaman, Department of Energy, University of Madras, Dr. R. Indrajit, Department of Physics, B.S. Abdur Rahman Crescent Institute of Science and Technology, Chennai and Dr. Gnanam, Department of Physics, Vels Institute of Science and Technology, Chennai for their invaluable guidance and persistent support in conducting this research.

Author Contributions D.S.N. performed conceptualization, experimental design, methodology, formal analysis and writing - original draft. S.D. performed review and editing Dr. S. A. contributed to discussion pertained to material selection. Dr. S.D. contributed to methodology and data validation. Dr. R.A.K. coordinating the research activity, including planning and data validation, supervision, project administration and funding acquisition. Dr. P. S. K. contributed to data validation. All authors reviewed the results and approved the final version of the manuscript.

Funding No funding obtained for this work.

Data Availability All data analyzed during the study are included in this article and will be made upon reasonable request.

Declarations

Ethical Approval Not applicable.

Informed Consent Not applicable.

Conflict of interest The author(s) declare that there is no conflict of interest regarding the publication of this article.

References

1. Goyal RN, Bishnoi S, Agrawal B (2011) Electrochemical sensor for the simultaneous determination of caffeine and aspirin in human urine samples. J Electroanal Chem 655(2):97–102
2. Cao C, Jin R, Wei H, Liu Z, Ni S, Liu GJ, Young HA, Chen X, Liu G (2020) Adaptive in vivo device for theranostics of inflammation: real-time monitoring of interferon-γ and aspirin. Acta Biomater 101:372–383
3. Suriyanarayanan S, Mandal S, Ramanujam K, Nicholls IA (2017) Electrochemically synthesized molecularly imprinted polythiophene nanostructures as recognition elements for an aspirin-chemosensor. Sens Actuators B 253:428–436
4. Syamala M, Srivastava D, Khandekar SD, Porselvi T, Patan MK, Balaram A, Kumaran S (2025) Construction of g-C3N4 anchored Cu-ZnS hybrid nanostructures for sustainable energy storage and environmental remediation. Res Chem Intermed 1–30
5. Mullangi R, Sharma K, Srinivas NR (2012) Review of HPLC methods and HPLC methods with mass spectrometric detection for direct determination of aspirin with its metabolite (s) in various biological matrices. Biomed Chromatogr 26(8):906–941
6. Wabaidur SM, Alothman ZA, Khan MR (2013) A rapid method for the simultaneous determination of l-ascorbic acid and acetylsalicylic acid in aspirin C effervescent tablet by ultra performance liquid chromatography–tandem mass spectrometry. Spectrochim Acta Part A Mol Biomol Spectrosc 108:20–25
7. Adomavičiūtė S, Velička M, Šablinskas V (2020) Detection of aspirin traces in blood by means of surface-enhanced Raman scattering spectroscopy. J Raman Spectrosc 51(6):919–931
8. Wang Y, Xu H, Zhang J, Li G (2008) Electrochemical sensors for clinic analysis. Sensors 8(4):2043–2081
9. Kumaran S, Navaneethan S, Nagalalli G, Kalaiarasi K, Dineshkumar M (2025) Fabrication of 2D rGO decorated In2O3 hybrid sensor for efficient NO2 detection. J Mater Sci: Mater Electron 36(7):448
10. Moscone D, D'ottavi D, Compagnone D, Palleschi G, Amine A (2001) Construction and analytical characterization of Prussian blue-based carbon paste electrodes and their assembly as oxidase enzyme sensors. Anal Chem 73(11):2529–2535
11. Sivagurunathan D, Padmapriya A, Devendiran M, Kalaivani RA (2025) Design and fabrication of nitrogen-and sulfur-doped carbon quantum dot-integrated Cobalt hexacyanoferrate hybrid sensor electrodes for enhanced dopamine detection. J Mater Sci: Mater Electron 36(3):184
12. Pournaghi-Azar MH, Habibi B (2007) Nickel hexacyanoferrate film immobilized on the aluminum electrode as an inorganic matrix for dispersion of platinum and some platinum alloys particles for electrocatalytic oxidation of methanol. J Electroanal Chem 605(2):136–144
13. Ghica ME, Carvalho RC, Amine A, Brett CM (2013) Glucose oxidase enzyme Inhibition sensors for heavy metals at carbon film electrodes modified with Cobalt or copper hexacyanoferrate. Sens Actuators B 178:270–278
14. Agarwal R, Sharma MK, Bhattacharyya K (2016) Prussian Blue-Manganese hexacyanoferrate nanocomposite as multifunctional high performance electrode material. ChemistrySelect 1(13):3562–3568
15. Zhang X, He P, Zhang X, Li C, Liu H, Wang S, Dong F (2018) Manganese hexacyanoferrate/multi-walled carbon nanotubes nanocomposite: facile synthesis, characterization and application to high performance supercapacitors. Electrochim Acta 276:92–101
16. Chen J, Liao L, Sun B, Song X, Wang M, Guo B, Ma Z, Yu B, Li X 2022 manganese hexacyanoferrate anchoring MnO2 with

enhanced stability for aqueous zinc-ion batteries. J Alloys Compd 903: 163833
17. Song Z, Liu W, Zhou Q, Zhang L, Zhang Z, Liu H, Zhao Z (2020) Cobalt hexacyanoferrate/MnO2 nanocomposite for asymmetrical supercapacitors with enhanced electrochemical performance and its charge storage mechanism. J Power Sources 465:228266
18. Venkatesh D, Gayathri GS, Muralidharan VP, Vasanthan S, Geetha S, Rajeswaran P, Karthik PS (2024) Synthesis of SnO2-ZnO heterojunction composites for effective degradation of methylene blue and chromium (VI) under solar light irradiation. Ionics 30(11):7323–7336
19. Sohal N, Maity B, Basu S (2021) Recent advances in heteroatom-doped graphene quantum Dots for sensing applications. RSC Adv 11(41):25586–25615
20. Gunjal DB, Nille OS, Naik VM, Shejwal RV, Kolekar GB, Gore AH (2023) Heteroatom/metal ion-doped carbon Dots for sensing applications. Carbon Dots in analytical chemistry. Elsevier, pp 181–197
21. Khayal A, Dawane V, Amin MA, Tirth V, Yadav VK, Algahtani A, Jeon BH (2021) Advances in the methods for the synthesis of carbon Dots and their emerging applications. Polymers 13(18):3190
22. Shalini AS, Shahanaz L, Rajeswaran P, Tamilarasan R, Kumaran S, Karthik PS (2024) Facile green synthesis of gelatin sodium alginate cerium oxide hydrogel nanocomposite and their photocatalytic and its biological applications. Chem Pap 78(5):3111–3123
23. Wazir AH, Khan Q, Ullah F, Yaqoob K (2025) Green synthesis of highly luminous lemon juice-based carbon Dots for antimicrobial assessment and fingerprint detection. Int J Mater Res 116(2):102–113
24. Sahu Y, Hashmi A, Patel R, Singh AK, Susan MABH, Carabineiro SA (2022) Potential development of N-doped carbon dots and metal-oxide carbon dot composites for chemical and biosensing. Nanomaterials 12(19): 3434
25. Xu Z, Sun Y, Xie J, Nie Y, Xu X, Tu J, Zhao X (2022) High-performance Ni/Fe-codoped manganese hexacyanoferrate by scale-up synthesis for practical Na-ion batteries. Mater Today Sustain 18:100113
26. Sivagurunathan D, Deepa S, Devendiran M, Kalaivani RA (2025) Design and fabrication of Punica granatum peel-derived NSCQD/iron hexacyanoferrate ternary composite for simultaneous detection of ascorbic acid, uric acid, and resorcinol Ionics: 1–18
27. Tang Y, Li W, Feng P, Zhou M, Wang K, Wang Y, … Jiang K (2020) High-performance manganese hexacyanoferrate with cubic structure as superior cathode material for sodium-ion batteries. Adv Funct Mater 30(10): 1908754
28. Ramki D, Dharmendira Kumar M, Siva Karthik P (2023) Nanohybrids of 1D Tin oxide (SnO2) nanotubes 2D-reduced graphene oxide (RGO) for improving photodegradation of cr (VI). J Mater Sci: Mater Electron 34(6):551
29. Thamizhazhagan P, Sivakarthik P, Balaji J (2021) Photocatalytic reduction of CO 2 into solar fuels using M-BTC metal organic frameworks for environmental protection and energy applications. Digest J Nanomaterials Biostructures (DJNB) 16(4):1263–1275
30. Li S, Qian G, He X, Huang X, Lee SJ, Jiang Z, Liu Y (2022) Thermal-healing of lattice defects for high-energy single-crystalline battery cathodes. Nat Commun 13(1):704
31. Saravanan KK, Ramanujum K, Kumaran S (2024) Synergistic design and fabrication of g-C3N4 decorated Ni-doped CeO2 nanocomposite: a highly efficient photo and electrocatalyst for enhanced energy storage and environmental remediation. Diam Relat Mater 142:110780
32. Li M, Sciacca R, Maisuradze M, Aquilanti G, Plaisier J, Berrettoni M, Giorgetti M (2021) Electrochemical performance of manganese hexacyanoferrate cathode material in aqueous Zn-ion battery. Electrochim Acta 400:139414
33. Maisuradze M, Li M, Aquilanti G, Plaisier J, Giorgetti M (2023) Characterization of partially Ni substituted manganese hexacyanoferrate cathode material. Mater Lett 330:133259
34. Ali U, Liu B, Jia H, Li Y, Li Y, Hao Y., … Wang C (2024) In Situ Fe-Substituted Hexacyanoferrate for high-performance Aqueous Potassium ion batteries. Small 20(4): 2305866
35. Han J, Xu C, Zhao J, Sun H, Zhang X, Wang G (2025) Active and passive high-entropy shell enabling high rate and durable sodium manganese hexacyanoferrate cathode for sodium ion batteries. J Power Sources 636:236577
36. Durairasan M, Karthik PS, Balaji J, Rajeshkanna B (2021) Enhanced visible light photocatalytic performance of WSe2/CNT hybrid photocatalysts that were synthesized by a facile hydrothermal route. Ionics 27(5):2151–2158
37. Dsouza SD, Buerkle M, Brunet P, Maddi C, Padmanaban DB, Morelli A, … Svrcek V (2021)The importance of surface states in N-doped carbon quantum dots. Carbon 183: 1–11
38. Durairasan M, Saravanan KK, Siva Karthik P (2021) Enhanced performance of dye-sensitized solar cell-based g-C3N4/Ag3PO4 hybrid composites as novel electrodes fabricated by facial hydrothermal approach. J Mater Sci: Mater Electron 32(5):5404–5414
39. Parveen N, Ansari SA, Ansari MZ, Ansari MO (2022) Manganese oxide as an effective electrode material for energy storage: a review. Environ Chem Lett 20(1):283–309
40. Shangguan Q, Chen Z, Yang H, Cheng S, Yang W, Yi Z, … Wu P (2022) Design of ultra-narrow band graphene refractive index sensor. Sensors 22(17): 6483
41. Daniel M, Mathew G, Anpo M, Neppolian B (2022) MOF based electrochemical sensors for the detection of physiologically relevant biomolecules: an overview. Coord Chem Rev 468:214627
42. Efimov IM, Vanyushkin NA, Gevorgyan AH (2024) The determination of the sensitivity of refractive index sensors. In Photonics 11(1): 56 MDPI
43. Mohiuddin I, Singh R, Kaur V (2023) Fabrication of mesoporous nanoprobe with molecularly imprinted fluorescent carbon Dots embedded within silica network for the selective and sensitive detection of aspirin in ground water samples. J Environ Chem Eng 11(1):109067
44. Jain B, Jain R, Jha RR, Bajaj A, Sharma S (2022) A green analytical approach based on smartphone digital image colorimetry for aspirin and Salicylic acid analysis. Green Anal Chem 3:100033
45. Gegenschatz SA, Chiappini FA, Teglia CM, de la Peña AM, Goicoechea HC (2022) Binding the gap between experiments, statistics, and method comparison: A tutorial for computing limits of detection and quantification in univariate calibration for complex samples. Anal Chim Acta 1209:339342
46. John J, Koshy RA, Krishnan H, Asok A (2024) Degradation of aspirin in a microbial fuel cell powered electro-fenton system using an etched graphite felt cathode. Electrocatalysis 15(1):143–158
47. El-Gohary AR, Galal A, Atta NF (2024) Novel electrochemical sensor for simultaneous determination of amlodipine, atorvastatin, and acetylsalicylic acid based on carbon nanotubes-ferrocene/nickel chromium oxide nanocomposite. Microchem J 200:110221
48. Kruanetr S, Prabhu R, Pollard P, Fernandez C (2015) Pharmaceutical electrochemistry: the electrochemical detection of aspirin utilising screen printed graphene electrodes as sensors platforms. Surf Eng Appl Electrochem 51:283–289
49. Diouf A, Moufid M, Bouyahya D, Österlund L, El Bari N, Bouchikhi B (2020) An electrochemical sensor based on Chitosan capped with gold nanoparticles combined with a voltammetric electronic tongue for quantitative aspirin detection in human physiological fluids and tablets. Mater Sci Engineering: C 110:110665

50. Deiminiat B, Razavipanah I, Rounaghi GH, Arbab-Zavar MH (2017) A novel electrochemical imprinted sensor for acetylsalicylic acid based on polypyrrole, sol-gel and SiO2@ Au core-shell nanoparticles. Sens Actuators B 244:785–795
51. Ghadimi H, Tehrani RM, Basirun WJ, Ab Aziz NJ, Mohamed N, Ab Ghani S (2016) Electrochemical determination of aspirin and caffeine at MWCNTs-poly-4-vinylpyridine composite modified electrode. J Taiwan Inst Chem Eng 65:101–109
52. Abo-bakr AM, Abd-Elsabour M, Abou-Krisha MM (2021) An efficient Novel electrochemical sensor for simultaneous determination of vitamin C and Aspirin based on a PMR/Zn-Al LDH/GCE. Electroanalysis 33(12): 2476–2489
53. Jayasri D, Narayanan SS (2007) Manganese (II) hexacyanoferrate based renewable amperometric sensor for the determination of butylated hydroxyanisole in food products. Food Chem 101(2):607–614
54. Yang X, Zhang W, Yang Y, Dong B (2025) Mechanism of NP@CQDs in the detection of quinolone antibiotics in food waste digestate filtrate based on fluorescence sensitization effect. J Environ Chem Eng 13(1):1